

A wide-field study of globular clusters in the nearest giant elliptical: Subaru/Suprime-Cam observations of Maffei 1*

Samuel Hinton^{1,2}, Ricardo Salinas³ Aaron J. Romanowsky^{4,5}, and maybe some others

¹School of Mathematics and Physics, University of Queensland, QLD 4072, Australia

²Australian Astronomical Observatory, North Ryde, NSW 2113, Australia

³Gemini Observatory

⁴Department of Physics & Astronomy, San José State University, San Jose, CA 95192, USA

⁵University of California Observatories, 1156 High Street, Santa Cruz, CA 95064, USA

Accepted ... Received ...; in original form ...

ABSTRACT

Lorem ipsum dolor sit amet, consectetur adipiscing elit. Sed condimentum ipsum faucibus sem elementum, eu consectetur risus consectetur. Praesent quis aliquam risus. Vivamus interdum et eros gravida rhoncus. Proin accumsan finibus pellentesque. Praesent et erat eu velit maximus condimentum. Integer ornare vestibulum dolor nec pretium. Suspendisse suscipit, metus sed consectetur pretium, ligula nunc mollis quam, id dapibus est tortor et massa. Mae- cenas maximus elit orci, sit amet tincidunt libero ultrices a. Nullam sit amet condimentum libero. Duis ullamcorper lorem in nisi gravida tincidunt. Aliquam erat volutpat. Sed vitae sem a elit mattis porttitor.

Key words: Galaxies: individual: Maffei 1 – Galaxies: star clusters

1 INTRODUCTION

Add some general remarks on globular cluster systems.

Maffei 1 is a giant elliptical galaxy (Maffei 1968; Spinrad et al. 1971) located at only 0.5° North of the Galactic plane. This position implies large obscuration by dust from the Galactic disc which has hampered the measurement of even the most basic parameters of the galaxy.

Give main results from the literature

Its particular relative position has also conspired against the study of its globular clusters (GCs). Studies of its globular cluster system (GCS) have produced only a handful of GC candidates (Davidge 2002; Buta & McCall 2003; Davidge & van den Bergh 2005), whereas for its luminosity ($M_V \sim -20.80$, Fingerhut et al. 2007), the size of its GCS should be comparable to the one of Cen A, hosting ~ 1300 GCs (Harris 2010).

In this paper we present the first wide-field study of the Maffei 1 GCS system using Subaru/SuprimeCam imaging. In Sect. 2 we present the imaging data used, as well as its reduction and photometry. In Sect. 3 we present the GCs selection, together with the derived properties of the GCS. Sect. 4 puts our results on a wider context, while Sect. 5 summarizes the work and give conclusions.

2 SUBARU/SUPRIME-CAM OBSERVATIONS AND DATA REDUCTION

Maffei 1 images were obtained using Suprime-Cam (Miyazaki et al. 2002) located on the Subaru telescope, Mauna Kea, Hawaii. Suprime-Cam comprises 10 CCD detectors separated by $\sim 15''$ covering a field-of-view of $34' \times 27'$ with a pixel scale of $0.2''$. SDSS r' , i' and z' -band images were obtained during the night of January 5th, 2011. Several short exposures were taken with a $\sim 1'$ dither pattern, totalling 385, 280, and 280 seconds in the r' , i' and z' -bands, respectively.

Suprime-Cam images reduction was conducted within the SD-FRED2 pipeline (Ouchi et al. 2004). Reduction steps include bias subtraction, flat-fielding, correction for atmospheric distortions, point spread function (psf) equalization (i.e. the normalization of the psf to a single shape across the detectors and exposures), sky subtraction, image alignment and finally, the combination of all exposures and detectors into single images. Final averaged images have a field-of-view of $\sim 37' \times 31'$ and a seeing quality of $0.72''$, $0.68''$ and $0.63''$, for r' , i' and z' , respectively. The field of view in z' is shown in Figure 1, and a detailed colour image of the galactic core is presented in Figure 2.

For the z' image set, which is used as the basis for the GC candidates identification given its higher image quality (see Sect. 3.1), a parallel alternative reduction process was adopted. The z' dataset not only provides the reddest band to pierce through the Galactic plane, but also contains the best seeing images. Even though the same SD-FRED2 pipeline was mostly used, a couple of the aforementioned reduction steps were skipped in order to maintain image manipulations that could alter the image quality to a minimum.

* Based on data collected at Subaru Telescope, which is operated by the National Astronomical Observatory of Japan.

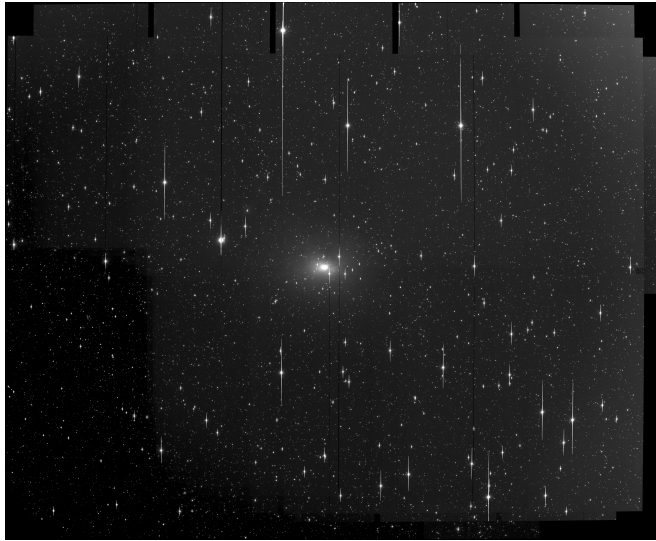


Figure 1. The Maffei 1 field as seen by Subaru-SuprimeCam in z' . Image size is approximately $37' \times 31'$. North is up and East is to the left.

Firstly, given the slight degradation of the psf towards the outer detectors, psf equalization across the chips would imply a loss of information on the best chips. For this reason the detectors were reduced independently and not combined into a single image as a final step. As a second difference, we did not apply any correction for atmospheric distortions, since it resulted in an increase of about 10% of the measured stellar full width at half maximum (fwhm) due to charge shifting to neighbor pixels. Finally, images with psf sizes significantly larger than the mean were excluded from the final image combination. This resulted in the rejection of zero to two exposures per chip.

Coordinate transformations and image combination for the individual detectors were carried out with DAOMASTER/MONTAGE2 (Stetson 1993, 1994), which give more flexibility than SDFRED2 for images with a small overlapping area. Measured fwhm on the combined z' images varies between $0.52''$ to $0.58''$ from detector to detector, which are noticeably better than the $0.62''$ measured on the combined full frame image given by SDFRED2.

As a last step prior to initial photometry, images presenting large background variations (containing Maffei 1 light or Galactic cirrus), were median filtered with an annulus kernel, with outer radius size of 150 pixel and an inner radius of 105 pixels; a large size that preserves point-like sources unaltered. Photometry and astrometry were performed on the images fully processed with the SDFRED2 pipeline.

2.1 Stellar photometry

Manual aperture and psf-fitting photometry were carried out on a chosen example tile using the stand-alone DAOPHOT2 photometric suite (Stetson 1987). The psf was modelled selecting ~ 120 – 140 bright and isolated stars on each detector. A quadratically varying Moffat function was found to provide the best description of the psf behaviour within the detectors.

Photometry for all the sources was also obtained using SExtractor (Bertin & Arnouts 1996), which additionally provides measurements of the size, orientation and ellipticity of the sources.

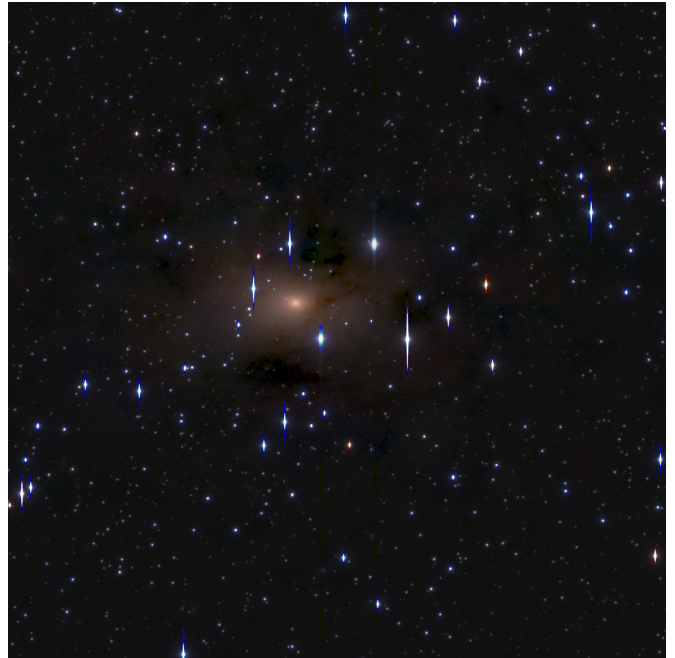


Figure 2. The core of Maffei 1 shown in z' , i' and r' , generated by STIFF (Bertin 2012). The image size is approximately $6.5' \times 6.5'$. North is up and East is to the left.

3 RESULTS

3.1 Selecting globular clusters candidates

The basic selection criterion for GCs in Maffei 1 rests on the non-stellar shape of their light profiles. This shape, usually smeared out for distant systems or in images with low spatial resolution, should be noticeable for the largest GCs in Maffei 1 given the galaxy's distance and the quality of the imaging. A similar approach has been applied successfully on ground-based imaging of GCs in the slightly more distant elliptical galaxy Centaurus A (Rejkuba 2001; Gómez et al. 2006; Gómez & Woodley 2007). As manual inspection of all sources was infeasible due to the number of sources, a machine learning approach was adopted in order to differentiate between stellar sources and extended sources. Initially, the neural network classifier contained inside SExtractor was utilised, but a posterior analysis has shown that clearly resolved sources have been assigned a CLASS_STAR parameter value as high as 0.98, which on a blind approach would have been classified as stars. Thus the algorithm was found to be insufficient, and a new algorithm was developed. Training of the machine learning algorithms was performed by combining artificially generated data and manual classification on a single tile.

Manual classification was performed by visual analysis of the star-subtracted z' -image of the chosen CCD tile produced by the psf-fitting algorithm in ALLSTAR. The image was visually inspected to look for residuals that revealed the presence of extended sources. The light profile of GCs (but also galaxies) would be over-subtracted in the central parts and under-subtracted in the wings, leaving an easily recognizable “ring-shaped” residual (see Fig. 3). A visual inspection of the residuals in a tile is a painstaking process, but provides benefit over only artificial data that does not model the full distribution of extended sources accurately. Our selected approach revealed the presence of 77 extended sources in the Clarisse tile.

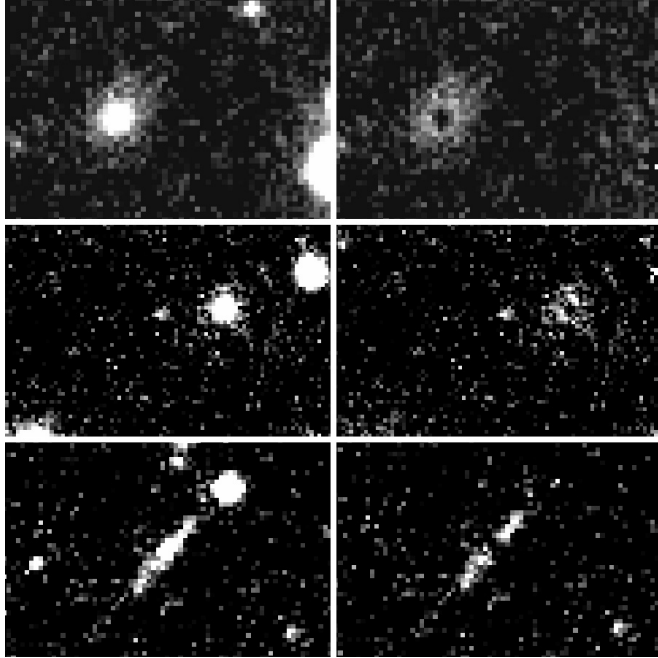


Figure 3. Three examples of the psf-subtraction technique applied on the final z images to reveal extended sources. The left panels show the original image, while the right panels are the psf-subtracted images. Top panels: A round object revealing a highly confident classification. Middle panels: A similar classification with a lower confidence due to the image noise. Bottom panels: An elongated extended object, in this case a galaxy viewed from the side, where the high ellipticity of the source allows differentiation between globular cluster and galaxy.

Artificial stars and extended sources were added to the Clarisse tile by the use of the `mksynth` task in BAOLAB (Larsen 1999). The psf input into the `mksynth` function was determined using by automatically selecting a number of candidate psf stars (based on flux criterion, star classification and source isolation), and generating a subsampled psf using the `digiphot` package in IRAF CITE. For generation of artificial extended objects, the `mkcmppsf` task was also used to generate a composite psf with a King model (King 1962) with concentration index of 30. The fwhm of the model was randomised to allow variation in the size of the artificial globular clusters. Both stars and extendeds were generated with uniform randomised magnitudes. The input data set was then created by using SExtractor to detect source properties of both the artificial sources and manually classified sources. In total, over 17 000 artificial globular cluster candidates and 170 000 artificial stars were introduced over a series of 300 artificial images to create a large set of data. The weighting of the manually detected stars and extended objects from the original tile was increased by a factor of a hundred to reflect their realism over artificial sources.

The input data was split into training, testing and validation sets, using ratios 0.4, 0.35 and 0.25 respectively, where multiple machine learning algorithms were trained on the training data, and the algorithm with the highest Matthews correlation coefficient (Matthews 1975) when evaluated on the validation set was selected as the final algorithm. The Matthews correlation coefficient was chosen to be maximised over other coefficients such as classifier accuracy, due to its fairness in dealing with unbalanced classes (Baldi et al. 2000; Jurman et al. 2012), which we expect to find with the number of point sources far exceeding the number of extended sources. Expected performance of the algorithm was determined

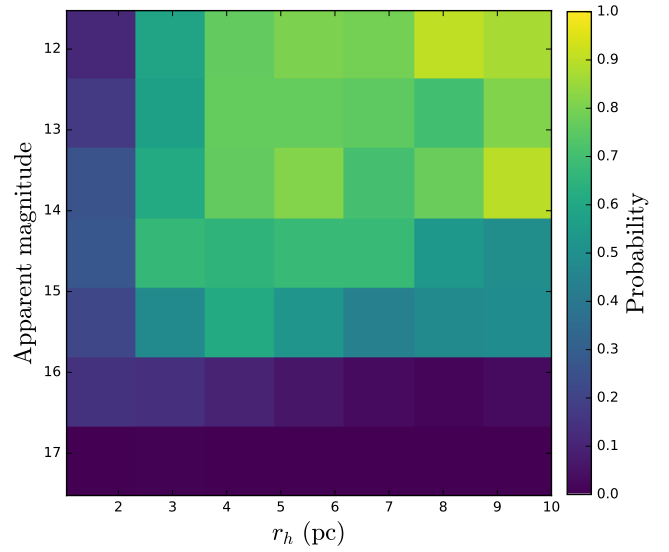


Figure 4. The probability $P(r_h, m_{z'})$ of correctly classifying an extended object using the initial classifier supplied with data from SExtractor. Classification accuracy decreases as r_h decreases, as the source becomes more pointlike. Similarly, we notice that objects dimmer than an apparent z' band magnitude of 16.5 are not classified correctly, as they are not detected by SExtractor. The maximum detection rate found corresponds to a 90% chance of detection.

by fitting to the test data set, and the probability of correctly classifying an extended object as a function of half light radius and magnitude is shown in Figure 4.

The extended candidates for each tile given by the initial machine learning algorithm were then processed through the task `iShape`, a procedure in the BAOLAB software package, to gather more information on the candidates. This step is done separately as computational constraints hinder the ability to run `iShape` on all detected sources, and so an initial candidate round must be selected. Information on χ^2 of the King fit, χ^2 of the delta model fit, and the fwhm of the King profile are added to the original data set. The manually selected candidates and artificially generated sources were also processed by `iShape`, and the improved dataset was used to train a second classifier in a similar fashion to the first, which was designed to remove many of the false positives from the initial classifier and improve accuracy on only partially resolved globular cluster candidates. The probability of detecting a source as a globular cluster correctly, as a function of half light radius r_h and magnitude for the new classifier is shown in Figure 5. It is important to note that the success rates shown in Figure 5 cannot be directly applied to the real data and thus only provide estimates. The matching accuracy on other tiles is expected to be lower due to artificial modelling not reflecting all the variations and subtleties of real global clusters and the lack of modelling other sources, such as compact dwarfs, stanard galaxies and other astronomical phenomenon outside stars and globular clusters.

Each candidate underwent aperture photometry on the fully reduced mosaics mentioned in Section 2, where colour magnitude corrections were performed by interpolating the dust maps from Schlegel et al. (1998) and applying the band extinction to reddening ratios from Schlafly & Finkbeiner (2011). Magnitude calibration was performed by using the Landolt set of standard stars (Landolt 1992) that had been transformed via the equations given in

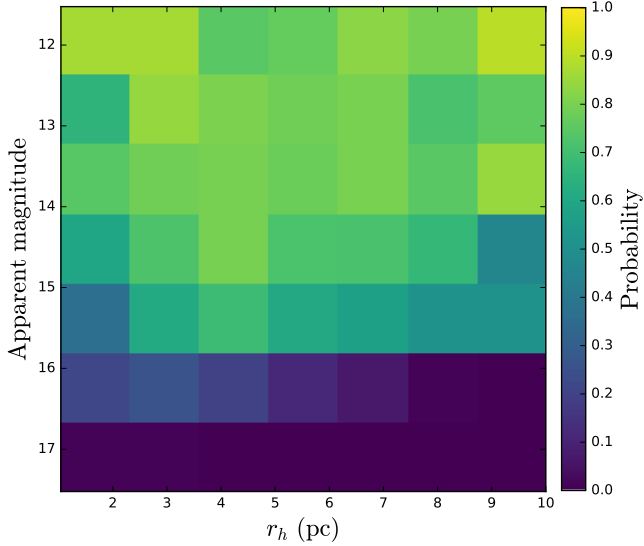


Figure 5. The probability $P(r_h, \mu)$ of correctly classifying an extended object using the secondary classifier, that is supplied with both data from SExtractor and data from ISHAPE fitting to a King profile. The fitting information allows increased discrimination between point sources and extended objects at lower values of r_h . The maximum chance of detection mirrors that found in Figure 4 at 90%.

Fukugita et al. (1996) into the SDSS system. Zero point magnitude calibrations were determined using the `fitparams` task in IRAF.

Further pruning of the globular cluster candidates was performed removing unphysical outliers in the analysis, such as removing objects with a detected fwhm of over a ten arcseconds. In addition, ellipticity cutoffs, colour profile cuts and magnitude cuts were introduced to remove galaxies in the globular cluster candidate list.

3.2 Globular clusters color-magnitude diagram

3.3 Globular cluster sizes

4 DISCUSSION

5 SUMMARY AND CONCLUSIONS

ACKNOWLEDGMENTS

AJR was supported by National Science Foundation grants AST-0808099 and AST-0909237.

REFERENCES

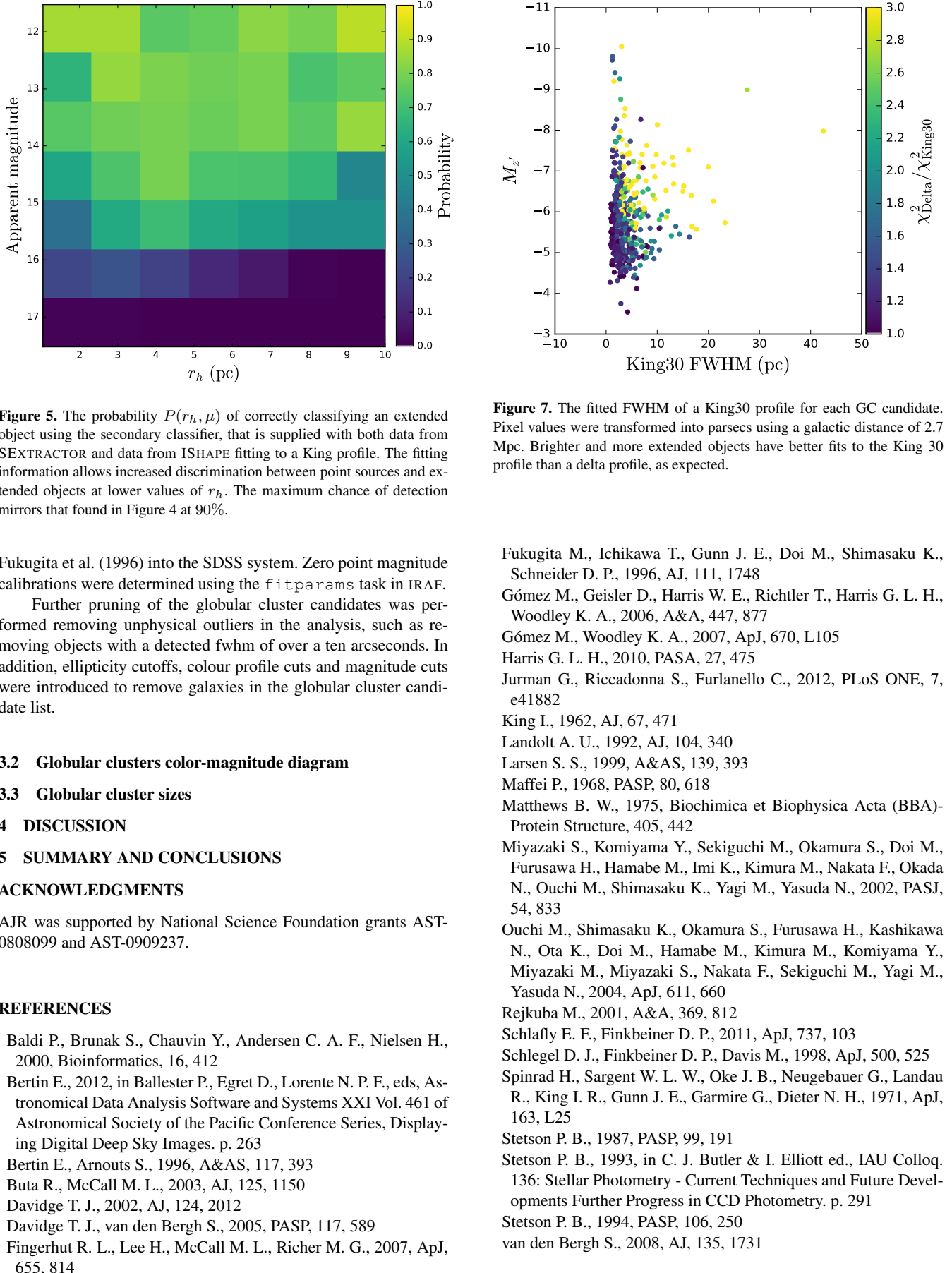


Figure 7. The fitted FWHM of a King30 profile for each GC candidate. Pixel values were transformed into parsecs using a galactic distance of 2.7 Mpc. Brighter and more extended objects have better fits to the King 30 profile than a delta profile, as expected.

- Fukugita M., Ichikawa T., Gunn J. E., Doi M., Shimasaku K., Schneider D. P., 1996, AJ, 111, 1748
 Gómez M., Geisler D., Harris W. E., Richtler T., Harris G. L. H., Woodley K. A., 2006, A&A, 447, 877
 Gómez M., Woodley K. A., 2007, ApJ, 670, L105
 Harris G. L. H., 2010, PASA, 27, 475
 Jurman G., Riccadonna S., Furlanello C., 2012, PLoS ONE, 7, e41882
 King I., 1962, AJ, 67, 471
 Landolt A. U., 1992, AJ, 104, 340
 Larsen S. S., 1999, A&AS, 139, 393
 Maffei P., 1968, PASP, 80, 618
 Matthews B. W., 1975, Biochimica et Biophysica Acta (BBA)-Protein Structure, 405, 442
 Miyazaki S., Komiyama Y., Sekiguchi M., Okamura S., Doi M., Furusawa H., Hamabe M., Imi K., Kimura M., Nakata F., Okada N., Ouchi M., Shimasaku K., Yagi M., Yasuda N., 2002, PASJ, 54, 833
 Ouchi M., Shimasaku K., Okamura S., Furusawa H., Kashikawa N., Ota K., Doi M., Hamabe M., Kimura M., Komiyama Y., Miyazaki M., Miyazaki S., Nakata F., Sekiguchi M., Yagi M., Yasuda N., 2004, ApJ, 611, 660
 Rejkuba M., 2001, A&A, 369, 812
 Schlafly E. F., Finkbeiner D. P., 2011, ApJ, 737, 103
 Schlegel D. J., Finkbeiner D. P., Davis M., 1998, ApJ, 500, 525
 Spinrad H., Sargent W. L. W., Oke J. B., Neugebauer G., Landau R., King I. R., Gunn J. E., Garmire G., Dieter N. H., 1971, ApJ, 163, L25
 Stetson P. B., 1987, PASP, 99, 191
 Stetson P. B., 1993, in C. J. Butler & I. Elliott ed., IAU Colloq. 136: Stellar Photometry - Current Techniques and Future Developments Further Progress in CCD Photometry. p. 291
 Stetson P. B., 1994, PASP, 106, 250
 van den Bergh S., 2008, AJ, 135, 1731

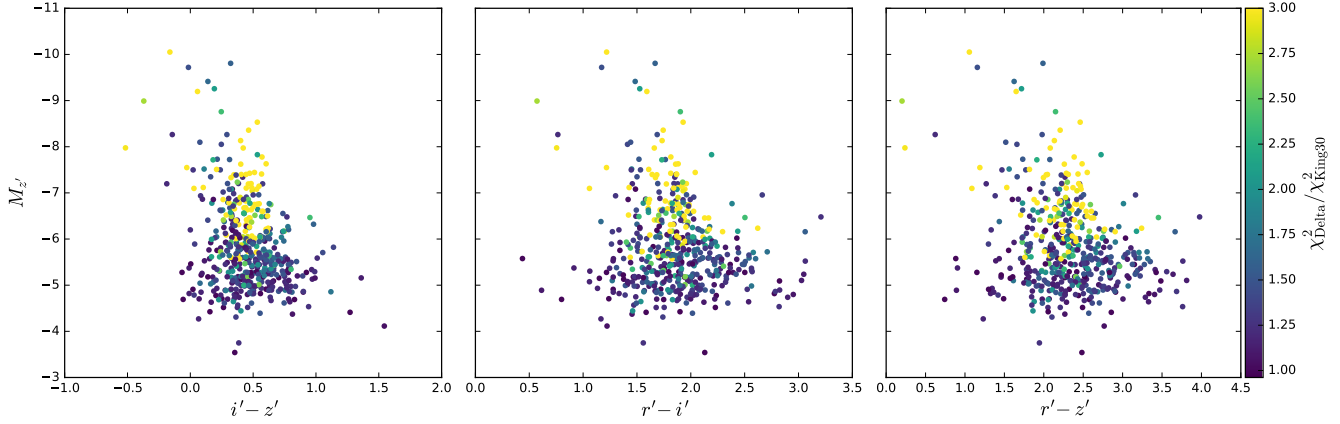


Figure 6. The determine colours of the GC candidates in the r' , i' and z' bands when applicable.
put something interesting here

Table A1. Photometry of the first ten “Class A” (see main text for its definition) globular cluster candidates. Absolute magnitudes have been computed using $D = 2.7$ Mpc.

ID	RA	DEC	ϵ	$M_{z'}$	$m_{z'}$	$r' - z'$	King ₃₀ FWHM (pc)
A1	39° 34' 26.472"	59° 53' 22.920"	0.03	-12.120	15.037	1.258	1.15
A2	39° 32' 11.832"	59° 52' 29.388"	0.10	-6.315	20.842	2.587	4.88
A3	39° 33' 13.680"	59° 52' 0.732"	0.07	-7.405	19.752	2.475	7.04
A4	39° 29' 7.800"	59° 51' 57.600"	0.25	-7.624	19.533	2.525	4.10
A5	39° 39' 9.540"	59° 51' 36.720"	0.17	-6.039	21.118	2.119	3.64
A6	39° 32' 39.048"	59° 50' 18.024"	0.20	-6.108	21.048	2.398	3.84
A7	39° 32' 41.100"	59° 50' 1.176"	0.24	-7.073	20.084	2.526	6.64
A8	39° 39' 18.360"	59° 49' 41.196"	0.10	-6.037	21.120	2.622	5.48
A9	39° 39' 14.544"	59° 49' 37.056"	0.16	-5.606	21.550	2.567	10.54
A10	39° 36' 51.912"	59° 49' 23.628"	0.17	-7.189	19.968	2.227	11.32

APPENDIX A: GLOBULAR CLUSTER CANDIDATES PHOTOMETRY

This paper has been typeset from a TeX/LaTeX file prepared by the author.

Table A2. Photometry of the first ten “Class B” globular cluster candidates. Absolute magnitudes have been computed using $D = 2.7$ Mpc.

ID	RA	DEC	ϵ	$M_{z'}$	$m_{z'}$	$r' - z'$	King ₃₀ FWHM (pc)
B1	39° 35' 27.204"	59° 54' 6.984"	0.07	-8.051	19.106	1.652	1.50
B2	39° 37' 49.872"	59° 53' 26.376"	0.22	-7.342	19.814	2.212	1.24
B3	39° 33' 14.724"	59° 53' 23.316"	0.13	-5.830	21.327	2.030	0.95
B4	39° 29' 59.280"	59° 53' 6.648"	0.23	-5.134	22.022	1.921	8.14
B5	39° 35' 49.848"	59° 52' 56.424"	0.08	-5.157	22.000	2.821	1.91
B6	39° 31' 38.388"	59° 52' 39.648"	0.10	-4.878	22.279	2.101	6.32
B7	39° 29' 15.288"	59° 52' 25.788"	0.19	-5.080	22.077	2.187	3.35
B8	39° 43' 37.632"	59° 51' 57.060"	0.18	-7.197	19.960	2.477	4.42
B9	39° 35' 8.916"	59° 51' 57.312"	0.02	-6.022	21.135	3.428	1.33
B10	39° 33' 59.148"	59° 51' 36.432"	0.05	-11.998	15.159	0.863	1.41